Electronic Supplementary Information

Staging Na/K-ion de-/intercalation of graphite retrieved from spent Li-ion batteries: in operando X-ray diffraction studies and advanced anode material for Na/K-ion batteries

Hao-Jie Liang,[a] Bao-Hua Hou,[a] Wen-Hao Li,[b] Qiu-Li Ning,[a] Xu Yang,[a] Zhen-Yi Gu,[b] Xue-Jiao Nie,[a] Guang Wang,[a] and Xing-Long Wu*[a,b]

[a] National & Local United Engineering Laboratory for Power Batteries, Faculty of Chemistry, Northeast Normal University, Changchun, Jilin 130024, P. R. China.

[b] Key Laboratory for UV Light-Emitting Materials and Technology, Northeast Normal University, Ministry of Education, Changchun, Jilin 130024, P. R. China.

* the corresponding author, e-mail: xinglong@nenu.edu.cn

1. Experimental methods

Recycling process for the exhausted graphite anode

Firstly, the exhausted graphite anode powder was manually scraped off and collected from the spent LIBs disassembled at the fully discharging state. Secondly, through stirring the collected anode powder in absolute ethanol and then centrifuging several times before drying at 60 °C for 24 hours, the RG can be obtained. Finally, the obtained RG was calcined at 700°C, 1000°C, 1300°C and 1600°C for 4 hours under Argon atmosphere to generate the RG-700, RG-1000, RG-1300 and RG-1600 samples.

Material characterizations.

The structure, morphology and composition of all obtained materials were characterized by X-ray diffraction (XRD, Rigaku SmartLab with 30 mA, 40 kV and λ = 1.5418 Å), Raman spectroscopy (JY HR-800 LabRam, at the 532 nm laser source), X-ray photoelectron spectroscopy (XPS, VG Scientific with 300 W Al Kα source), scanning electron microscope (SEM, HITACHI-SU8010) and high-resolution transmission electron microscopy (HRTEM, JEOL-2100 F, 200 kV).

Electrochemical measurements.

The electrochemical performances of active materials were tested in the 2032-type coin cells. The working electrodes with the active materials, carbon black and carboxymethyl cellulose sodium (CMC) at the mass ratio of 7:2:1 in distilled water were prepared by coating the slurry on the Cu/Al foil as the current collector. All working electrodes were dried in a vacuum oven for 12 hours at 60 ^{o}C. The Na/K-ion half cells were assembled in the glove box filled with high-pure Argon. The counter electrodes were metallic Na or K foils for the NIBs or KIBs,

respectively. Glass filter (Whatman 934AH) was used as the separator for both batteries. 1.0 mol L^{-1} $NaCF_3SO_3$ in diethylene glycol dimethyl ether (denoted by DEG-DME) was used as the electrolyte in Na-ion half cells, while 0.8 mol L^{-1} KPF_6 in ethylene-carbonate (EC): diethyl-carbonate (DEC) (1:1 in volume) was used as the electrolyte in K-ion half cells. The galvanostatic charge/discharge tests were conducted on the LAND-CT2001A in the potential range of 0.01-2.8 V or 0.01-2 V for NIBs or KIBs, respectively. CV profiles at various scan rates were collected on the electrochemical workstation (CHI 750E). The GITT measurements were performed at 0.02 mA g^{-1} (τ = 0.5 h, relaxation period: 4 hours) on the Arbin Instrument.

2. Structural characterizations

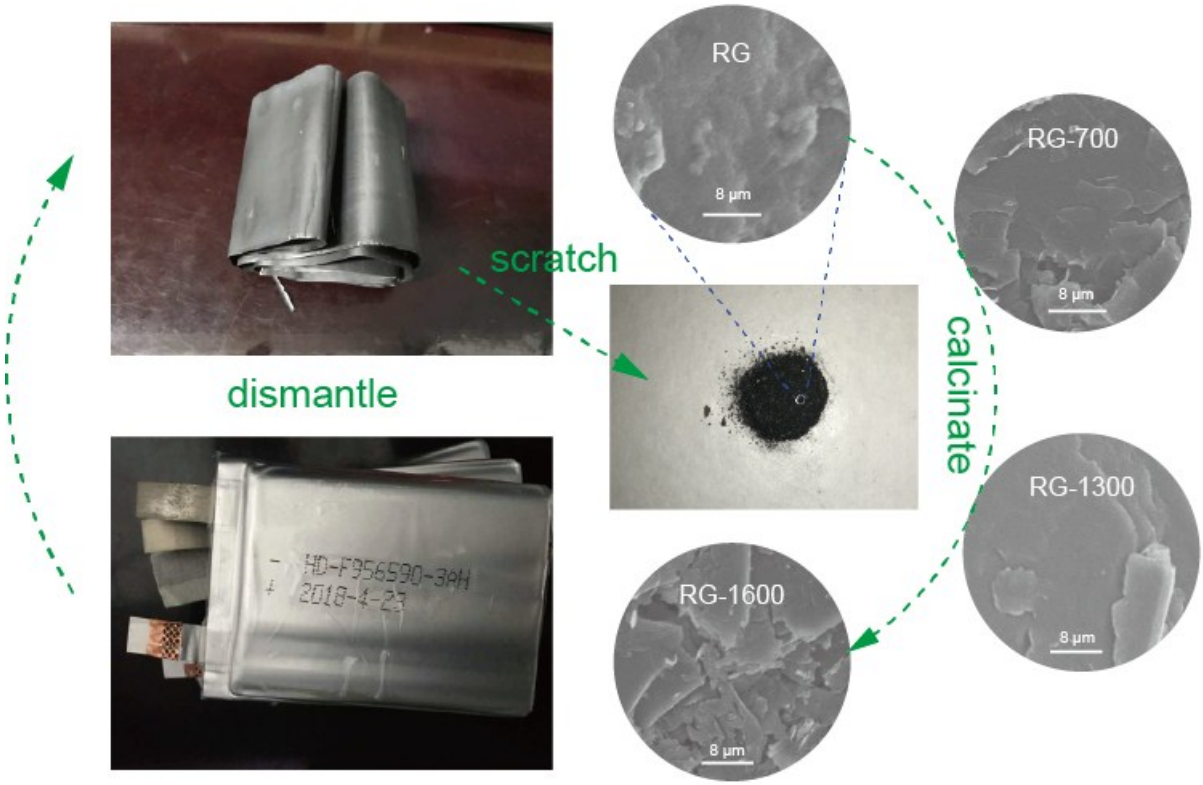

Fig. S1 Schematic illustration for the recycling procedures of the exhausted graphite anode material derived from the spent LIBs.

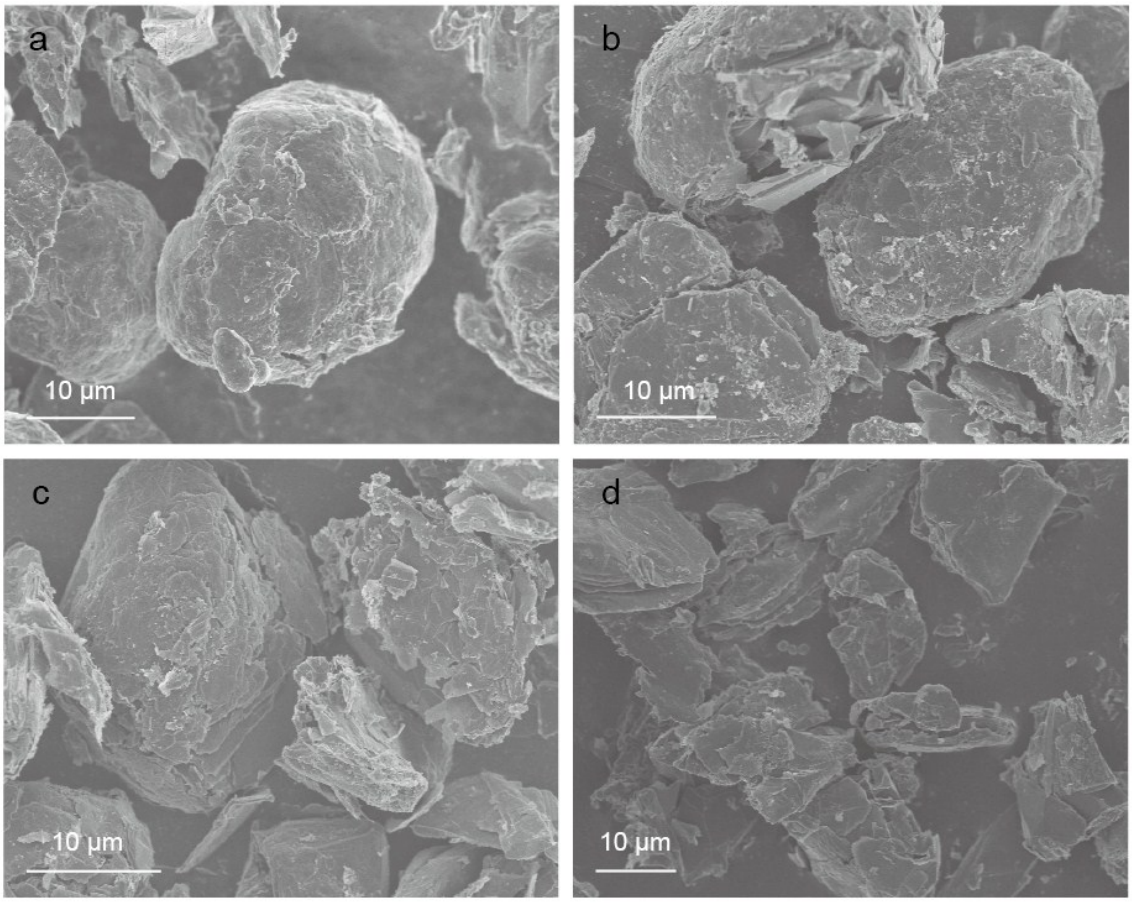

Fig. S2 SEM images of the a) RG, b) RG-700, c) RG-1300 and d) RG-1600 samples. As can be observed, the surface of RG is relatively smooth and unwrinkled. In contrast, apparent lamellar morphology can be observed in the RG-700, RG-1300 and RG-1600 obtained after the thermal calcination. The main particle size for all samples is around 20-30 μm, which is the typical size of the commercially available NMG anode.

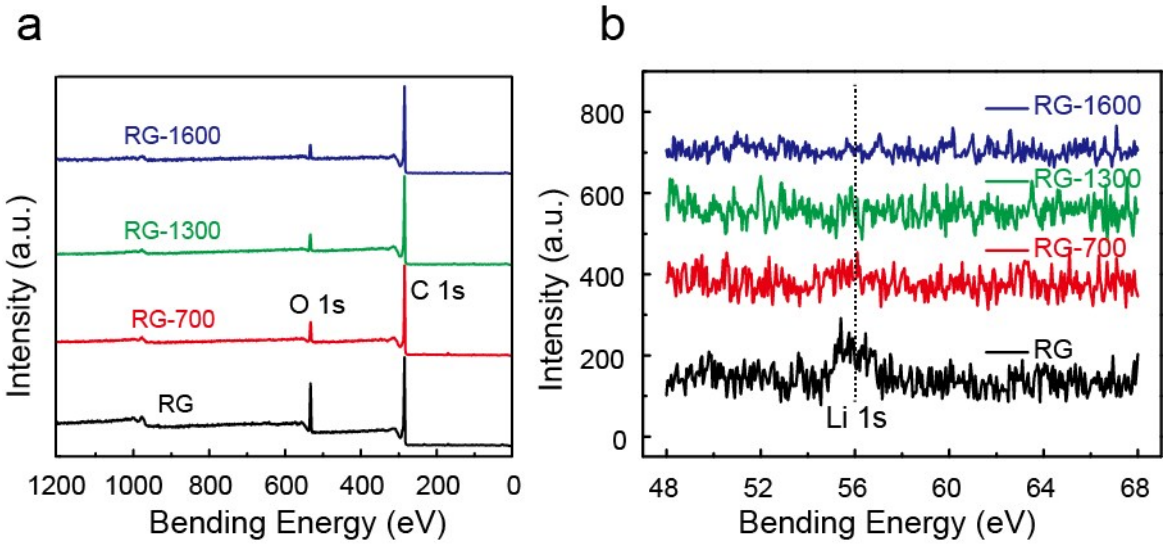

Fig. S3 (a) Full-scale X-ray photoelectron spectra and (b) Li 1S deconvoluted XPS spectra of the RG, RG-700, RG-1300 and RG-1600 samples.

Content of each element is as follows: (unit: at%)

species	C	O	F	Li
RG	83.63	13.57	1.6	1.2
RG-700	90.12	9.19	0.45	0.24
RG-1000	91.2	8.7	0.1	
RG-1300	91.91	8.09		
RG-1600	96.15	3.85		

As shown in Figure S3b, Figure S8d and above table, it is concluded that lithium content is little in in the cycled graphite after cycling (1.2 at%) and it nearly disappear through a pyrolysis process. For RG-700, only 0.24 at% can be detected, and the content of Li can't be detected for RG-1000, RG-1300 and RG-1600. Therefore, the impurities would hardly affect the electrochemical performances of the graphite anodes in NIBs or KIBs.

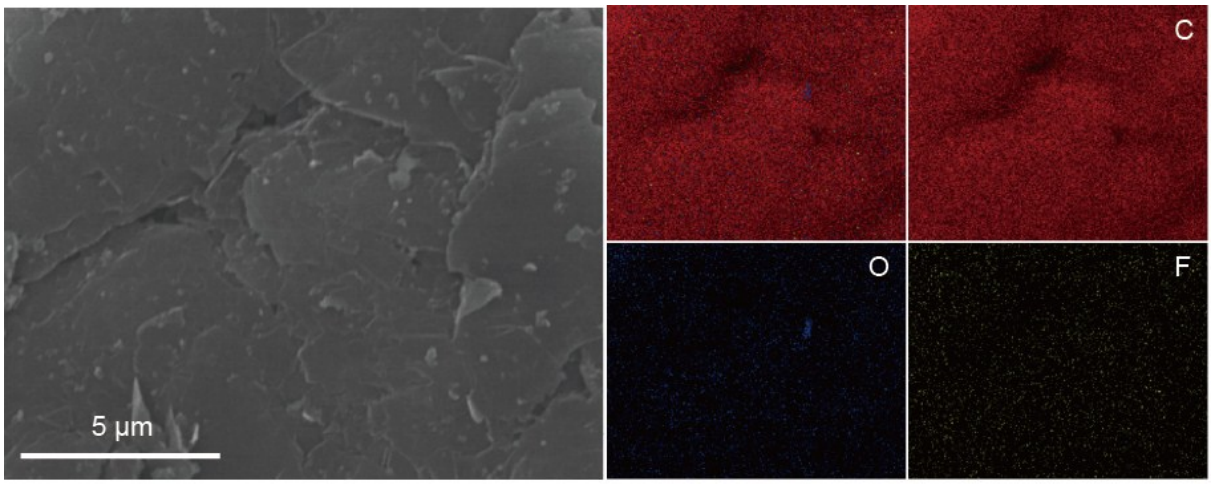

Fig. S4 SEM image and the corresponding EDS mapping of RG-1300. The EDS images display the homogeneous distribution of C, O and F (originated from the carbonization of PVDF binder) elements with the highest C content.

3. Electrochemical performance

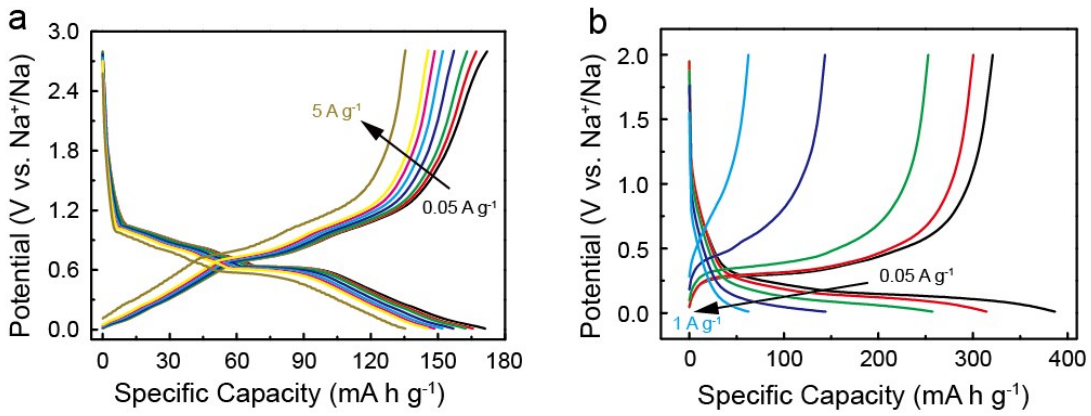

Fig. S5 GCD curves at different current densities of RG-1300 anode material in (a) Na-ion half cells (from 0.05 A g^{-1} to 5 A g^{-1}) and (b) K-ion half cells (0.05 A g^{-1} to 1 A g^{-1}).

The initial Coulombic efficiencies of RG-1300 for NIBs and KIBs are about 90 % and 64 %, respectively.

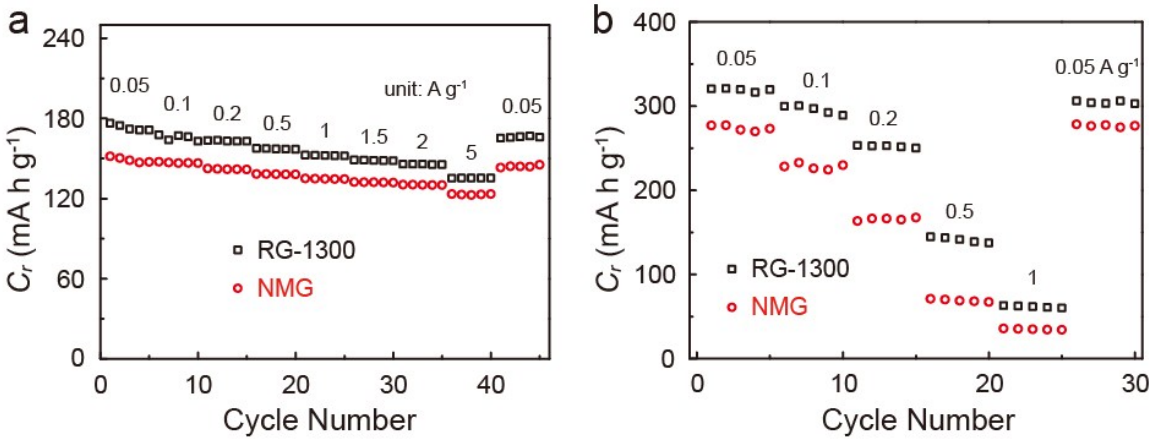

Fig. S6 Comparison of rate capability between RG-1300 and natural modified graphite (NMG) anode in (a) Na-ion half cells and (b) K-ion half cells.

The RG-1300 delivers the better electrochemical performance compared with NMR. This might be that the interlayer distance is enlarged through a pyrolysis process, and hence oxygen-containing functional group is stabilized through a series of variation. In addition, the irreversible defects gradually disappear.

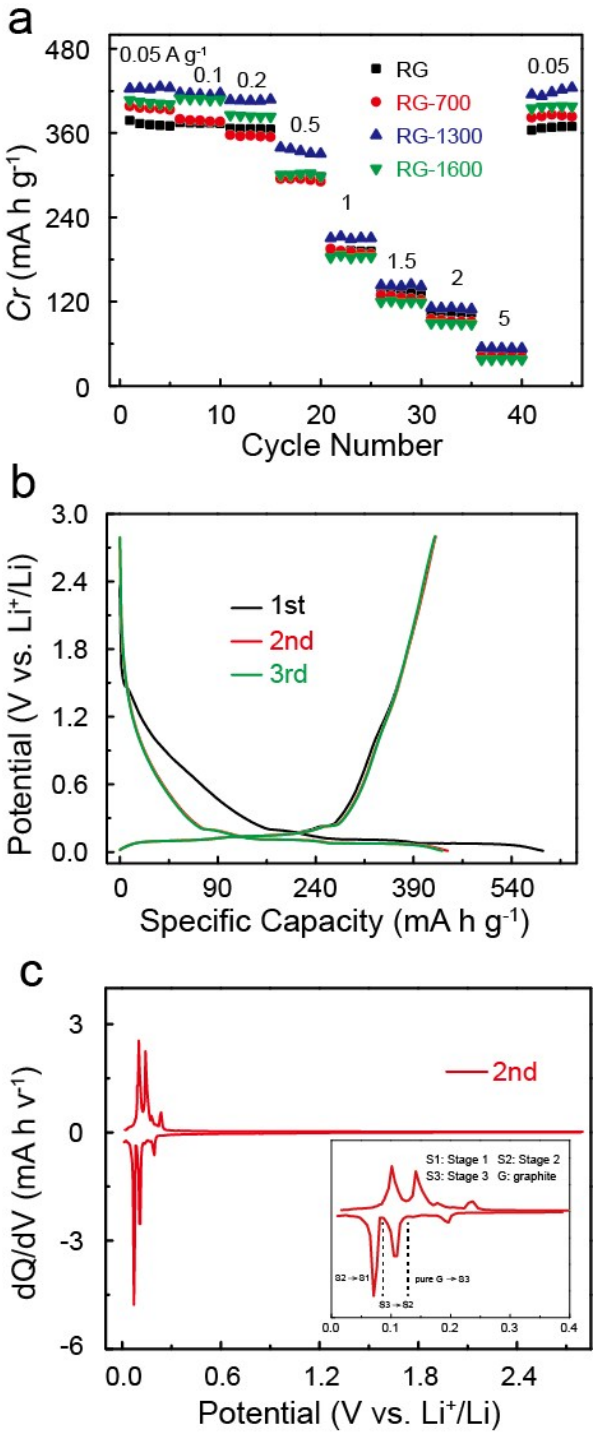

Fig. S7 (a) GCD curves of the initial three cycles at a low current density of 0.05 A g^{-1} for RG-1300, (b) rate capability comparison in LIBs at various current densities from 0.05 A g^{-1} to 5 A g^{-1}, and (c) differential capacity profiles of the second cycle of the RG-1300 electrode in LIBs (inset: the partly enlarged view between 0.01 V and 0.4 V.

When used in LIBs as shown in Figure S7, the RG-1300 delivers the best rate capability with the reversible capacities of 425, 415, 406, 334, 211, 142, 111 and 54 mA h g^{-1} at the current

densities of 0.05, 0.1, 0.2, 0.5, 1, 1.5, 2 and 5 A g^{-1} (Fig. S7a), respectively, which are the best electrochemical performance compared with other samples. As is well-known to us, the theoretical capacity of graphite anode is 372 mA h g^{-1}. The slightly larger C_r values delivered by recycled graphite than the theoretical one should be due to the additional Li storage at the reversible sites including the stabilized oxygen-containing functional group, defects generated during the battery usage, and enlarged interlayer distance between graphene layers.[S1-5] These sites are impossibly existed in a perfect graphite with theoretical Li storage of 372 mA h g^{-1}.

Figure S7b shows the GCD curves of the initial three cycles at a low current density of 0.05 A g^{-1} for the RG-1300 electrode. There is an obvious difference between the first discharge branch and the subsequent cycles with the well overlapping patterns. Such a difference should be from the formation of solid-electrolyte interphase (SEI) layers, which has been extensively reported in previous studies. In addition, although the typical stage patterns are not clear enough in the GCD curves, the corresponding differential capacity (dQ/dV) profiles give the distinct Li-insertion/extraction processes with the stage steps (Figure S7c).

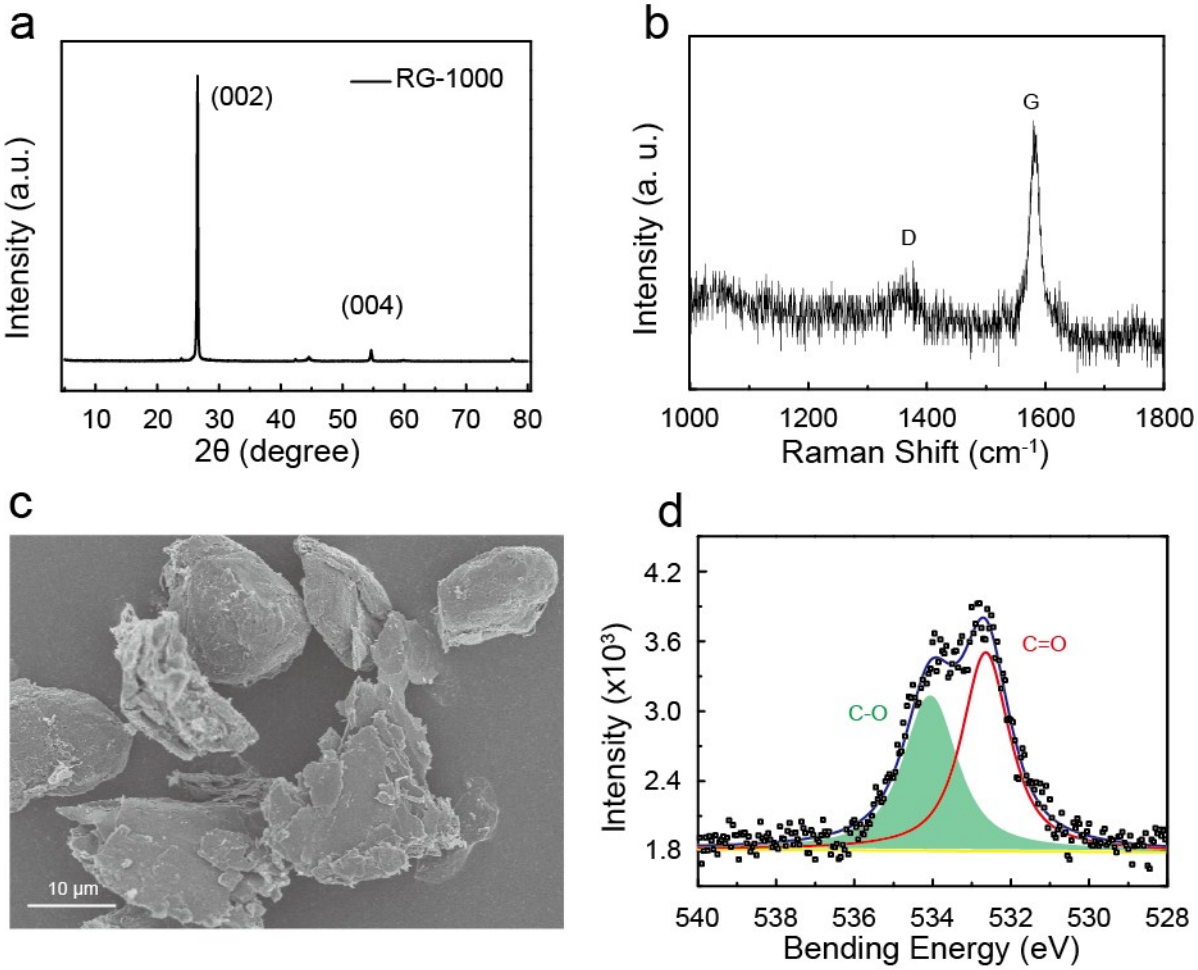

Fig. S8 Compositional and structural characterizations for the RG-1000: (a) XRD pattern, (b) Raman spectrum, (c) SEM image, and (d) the deconvoluted XPS spectrum of O1s.

Through above characterizations, the detailed information is as followed: The RG-1000 have an interlayer space of 3.360 Å for the (002) plane, the graphitized intensity ratio (I_D/I_G) of 0.48, and the intensity ratios ($I_{C\text{-}O}/_{C=O}$) of 0.78. It can be concluded that the structural features of RG-1000 is between RG-700 and RG-1300.

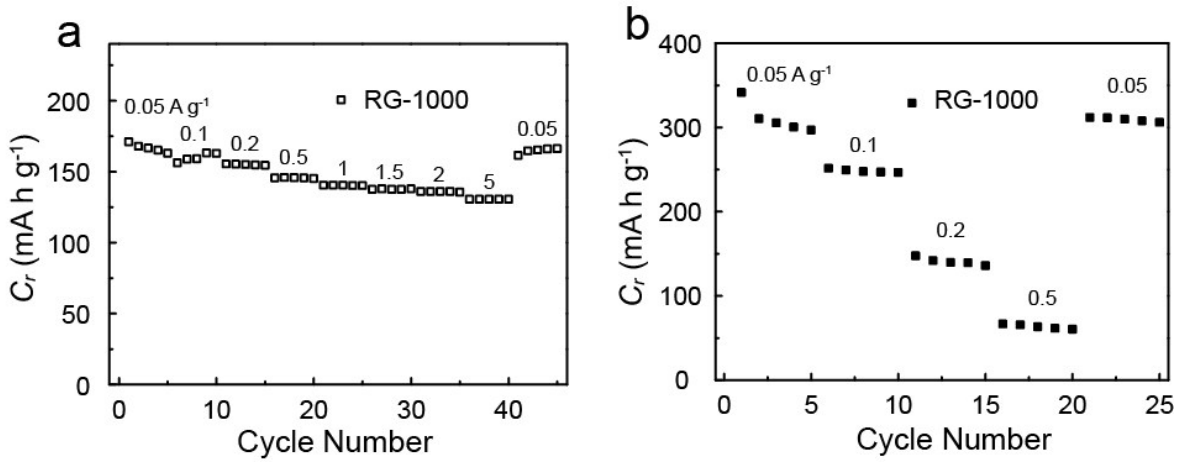

Fig. S9 Rate capability of the RG-1000 electrode (a) in Na-ion half cells at varied current densities of 0.05-5 A g^{-1} and (b) K-ion half cells at varied current densities of 0.05-0.5 A g^{-1}.

RG-1000 delivers the reversible capacities of 165, 158, 154, 145, 140, 137, 135 and 130 mA h g^{-1} at the current densities of 0.05, 0.1, 0.2, 0.5, 1, 1.5, 2 and 5 A g^{-1}, respectively, when used for NIBs. For KIBs, RG-1000 delivers the reversible capacities of 304, 251, 150, and 72 mA h g^{-1} at the current densities of 0.05, 0.1, 0.2 and 0.5 A g^{-1}, respectively. Compared these data with the samples of RG-700, RG-1300 and RG-1600, RG-1300 still exhibits the best electrochemical properties in both NIBs and KIBs.

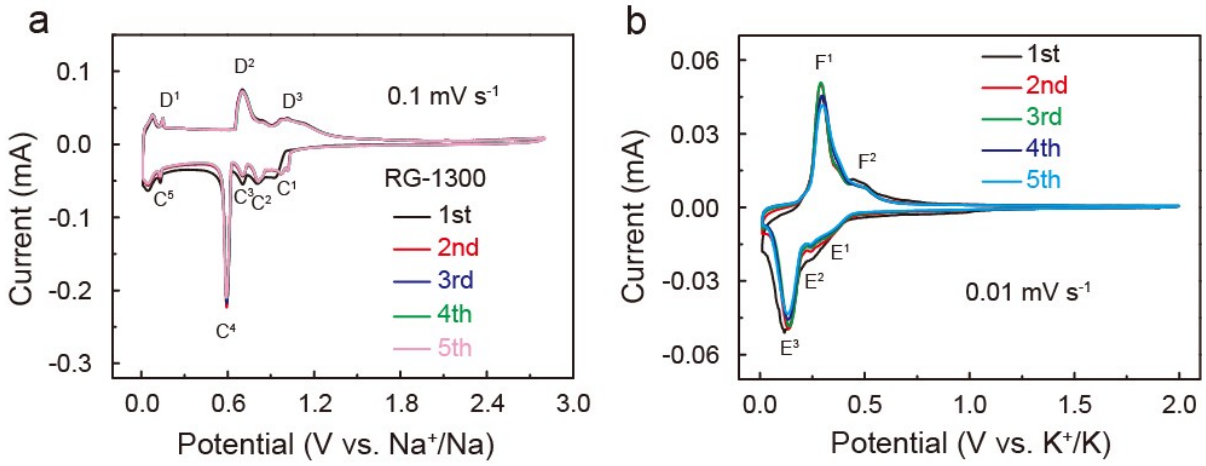

Fig. S10 CV curves of the initial five cycles for the RG-1300 electrodes in (a) Na-ion half cells and (b) K-ion half cells.

For Na-ion half cells, CV curves of the RG-1300 electrode present the slightly different cathodic peaks ascribed to the decomposition of electrolyte and the formation of SEI layer during the first cycle. In the following cycles, cathodic peaks located at 0.95, 0.8, 0.7, 0.6 and 0.2 V (denoted as C^1, C^2, C^3, C^4 and C^5) and anodic peaks located at 0.23, 0.72 and 0.98 V (denoted as D^1, D^2 and D^3) are observed, in which the prominent redox peaks (0.6/0.72 V) corresponding to plateau in Figure 2a are generally regarded as a result of insertion/extraction of solvated Na-ion in/out graphite interlayer, but electrochemical behavior corresponding to other peaks are uncertain. For K-ion half cells, there are a pair of prominent cathodic/anodic peaks (E^3/F^1) in low potential area but a series of inconspicuous redox peaks in high potential area, as a result of K-ion intercalation/deintercalation.

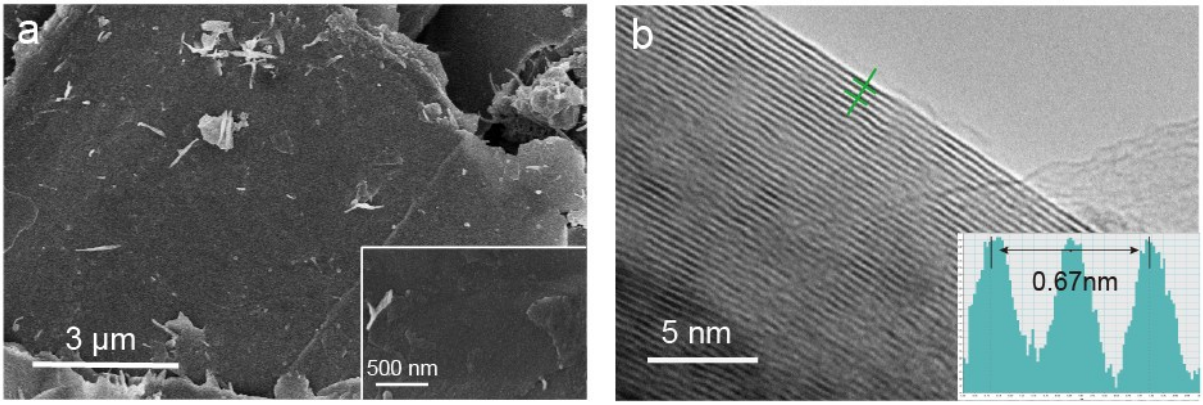

Fig. S11 SEM and TEM images of RG-1300 anode after 100 cycles at 2 A h g^{-1} in Na-ion half cells.

4. The *in operando* X-ray diffraction measurement details and supplementary date in Na/K-ion half cells.

The electrochemical cells applied in *in operando* X-ray diffraction measurement were designed and matched with the Rigaku SmartLab X-ray diffractometer (Cu-Kα, λ = 1.5418 Å).[S6] The working electrodes were prepared with RG-1300, PVDF and carbon black (the mass ratio is 7:2:1). Then the electrodes were vacuum-dried at 100 °C for 24 hours before assembled with thin Al-foil served as XRD window and current collector similar to the assemblage of Na/K-ion half cells. For Na-ion half cells, the RG-1300 electrodes were selected as 10 mg and pressed with 2T pressure after dried. For K-ion half cells, the weight was 4 mg and would not be pressed due to the slow kinetics.

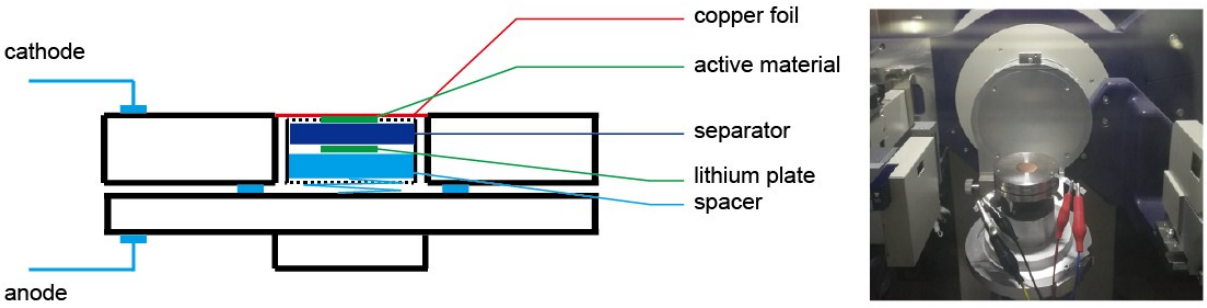

Fig. S12 Schematic diagram for *in operando* XRD measurement device.

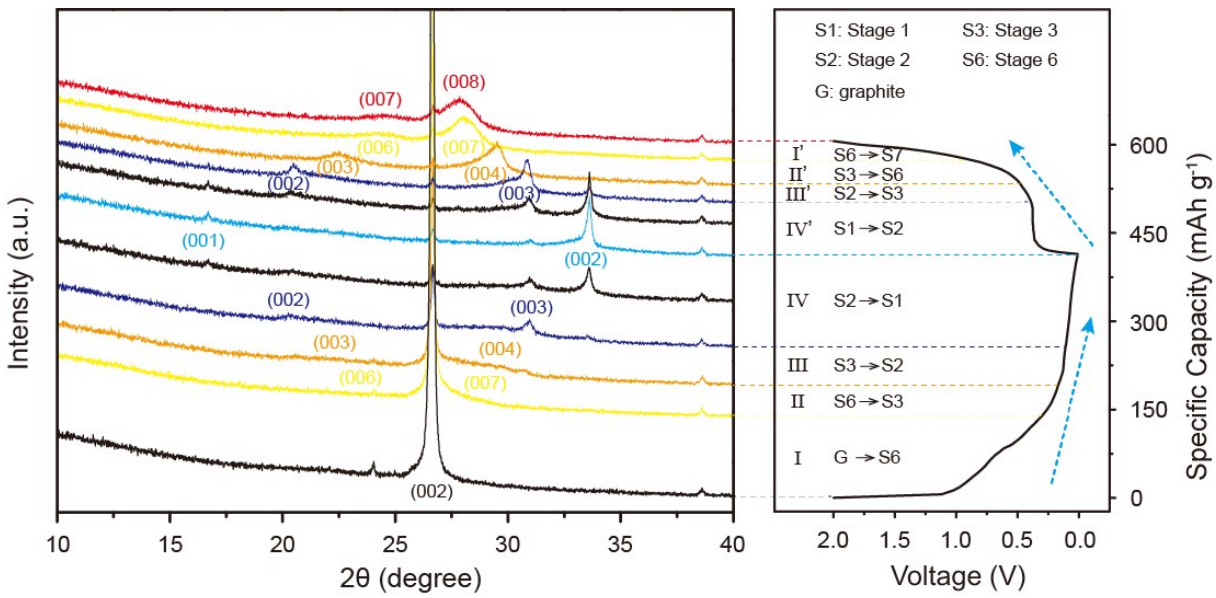

Fig. S13 The simplified staging *in operando* XRD profiles with the discharge and charge curves of the first cycle at 0.06 A g^{-1}.

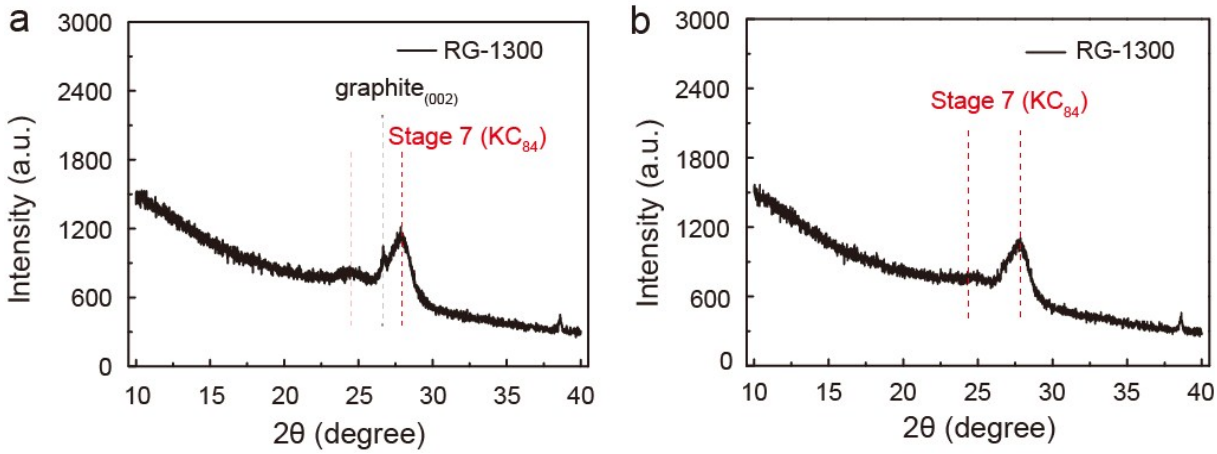

Fig. S14 *In operando* XRD pattern of RG-1300 when (a) charged to 2.8 V at the end of the first cycle and b) 2 V at the end of the third cycle.

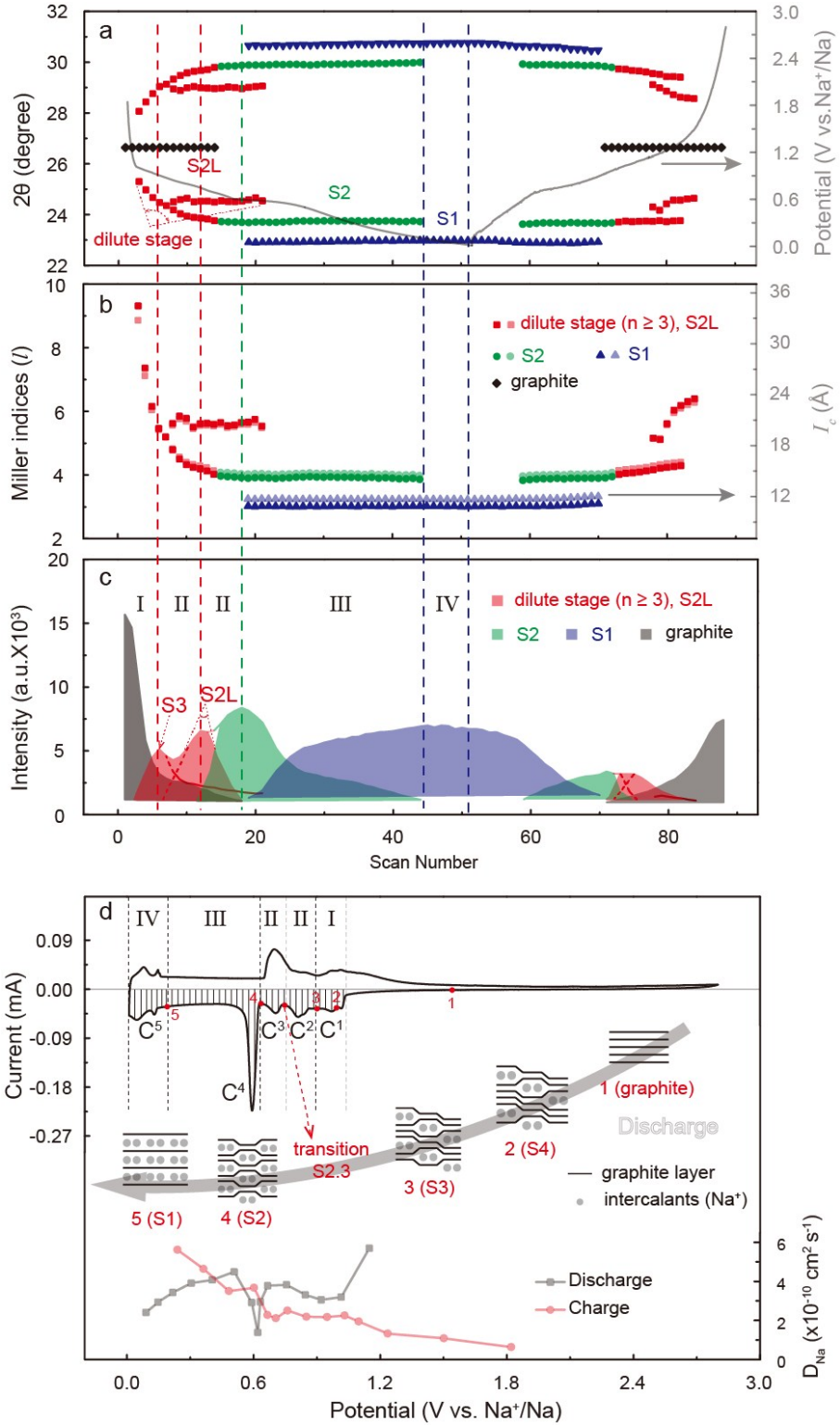

Fig. S15 (a-c) Variations of *in operando* XRD peak positions, Miller indices, I_c values and multiple de-/intercalation stage evolution (based on the intensity of (00*l*) peaks in the range of 20-27°) in the Na-ion half cells during the second GCD cycle. (d) the relational graph including CV profiles and the apparent Na^+-diffusion coefficients calculated from GITT tests illustrating the stage transformation during Na-ion de-/intercalation.

For the Na-ion de-/intercalation of RG-1300, **Fig. S15a** and **15b** shows the variation of

XRD peak positions, the Miller indices, and I_c values with the scan number of *in operando* XRD in the second cycle. The relevant staging phase transition is depicted in **Fig. S15c**, in which the ordinate values are the corresponding intensity of (00*l*) peaks. According to the analysis results, the discharging process can be divided into three regions: the red region in 2θ = 25.3-23.62°, the green region in 2θ = 24.57-24.54°, and the blue region in 2θ = 22.97-22.92° (Table S2 in the Supporting Information), clearly showing the staging intercalation mechanism: graphite → Stage 4 → Stage 3 → Stage 2.3 → Stage 2 → Stage 1. In addition, structural illustrations of different stages are also displayed in **Fig. S15d**.

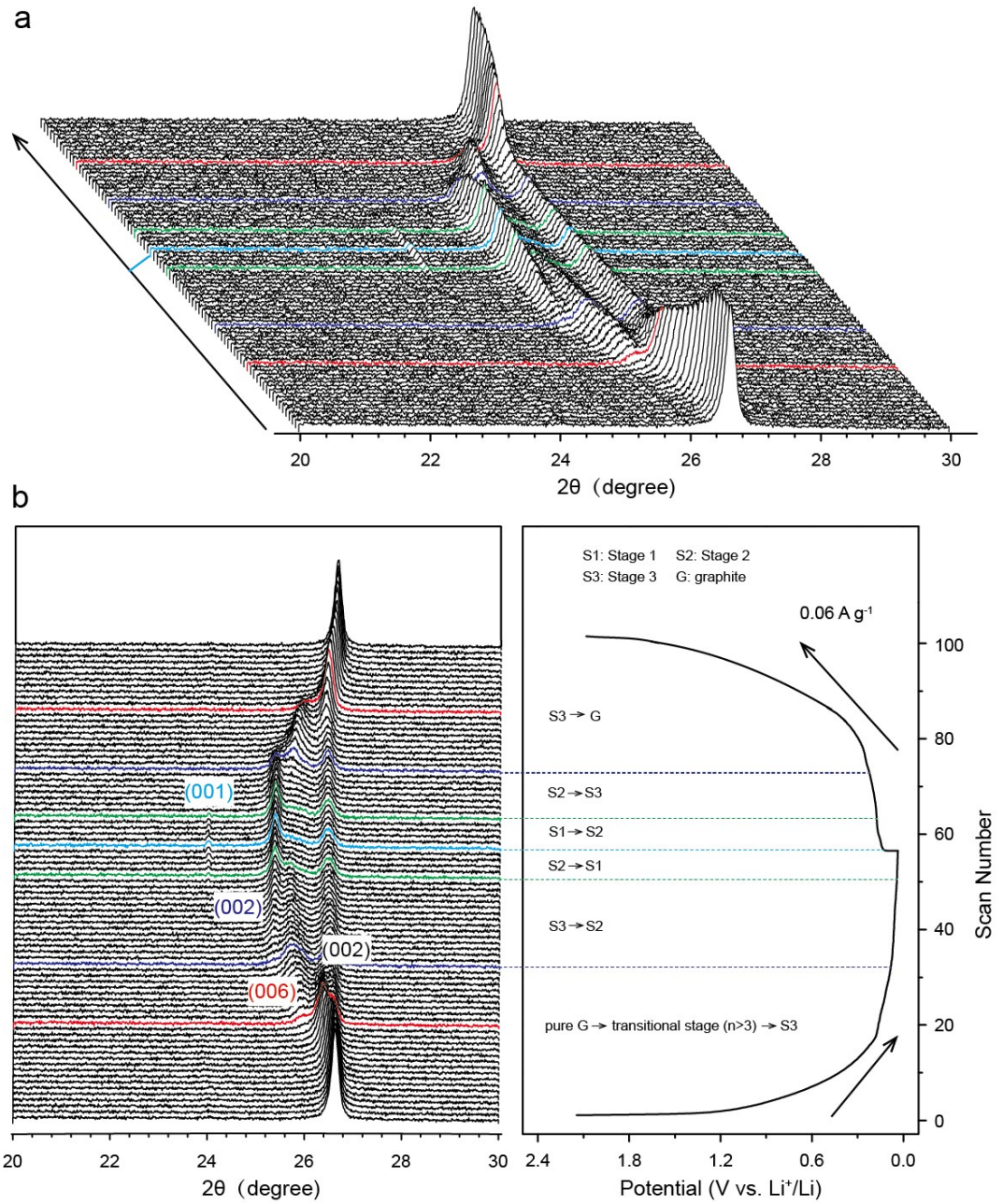

Fig. S16 *In operando* XRD patterns and analyses for the structural evolution during the electrochemical de-/intercalation of Li^+ in Li-ion half cells (the second GCD cycle): (a) the originally collected XRD patterns, (b) the simplified staging profiles attached with GCD curve at 0.06 A g^{-1}.

This is a typical graphite layer intercalation/deintercalation process which contains main three status: stage 1 (LiC_6, d = 3.7 Å), stage 2 (LiC_{12}, d = 3.52 Å), and stage 3 (LiC_{30}, d = 3.47 Å). Through test, the staging intercalation mechanism is demonstrated: graphite →transitional stage (n>3) → Stage 3 → Stage 2L (transitional stage) → Stage 2 → Stage 1. Due to the slightly

high current density, the peak intensity (001) of stage 1 is not distinct and the graphite peak remains, but the entire staging process is intact and accurate.

Table S1. Comprehensive stage evolution during the second discharge process in K-ion half cells (c: transitional stage is in a state of continuous change, ct: transitional stage stably exists, s: integer stage stably exists).

section	status	stage	process	Potential range	CV peak
I	c	stage 6≥n≥5	stage 7→stage 6	1-0.32 V	E^1
II	c	stage 6>n≥3	stage 6→stage 3	0.32-0.2 V	E^2
III	ct	stage 2L stage 2	stage 3→stage 2L stage 2L→stage 2	0.2-0.12 V	E^3
IV	s	stage 2 stage 1	stage 2→stage 1	0.12-0.01 V	E^3

Table S2. Comprehensive stage evolution during the second discharge process in Na-ion half cells (c: transitional stage is in a state of continuous change, ct: transitional stage stably exists, s: integer stage stably exists).[S7-S10]

section	status	stage	process	Potential range	CV peak
I	c	stage n≥3	graphite→stage4 →stage 3	1-0.87 V	C^1
II	ct	stage 2L	stage 3→stage 2L	0.87-0.75 V	C^2
	ct	stage2	stage 2L→stage 2	0.75-0.62 V	C^3
III	s	stage 2 stage 1	stage 2→stage 1	0.62-0.25 V	C^4
IV	s	stage 1		0.25-0.01 V	C^5

5. The reaction kinetics of the RG-1300 electrode applied in Na/K-ion half cells

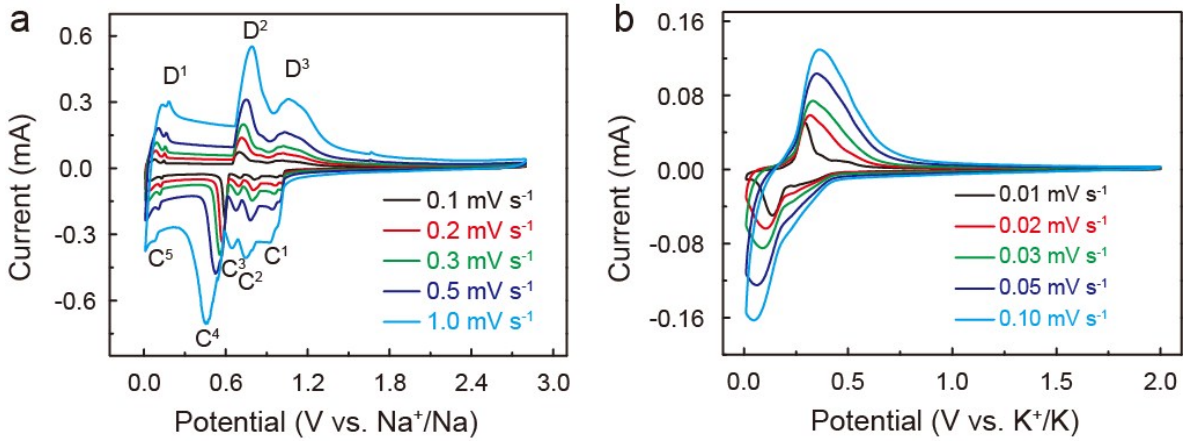

Fig. S17 CV curves of RG-1300 at different scan rate (0.1, 0.2, 0.3, 0.5, 1 mV s^{-1}) applied in a) NIBs and b) KIBs.

The apparent diffusion coefficient (D_{Na}) for solvated Na-ion derived from CV curves analysis was estimated by using the following equations:

$$I_p = 2.69 \times 10^5 n^{3/2} A D^{1/2} v^{1/2} \Delta C_o \qquad S1$$

$$C_n + e^- + A^+ + ysolv \leftrightarrow A^+(solv)_y C_n^- \qquad S2$$

Where I_p and v is the peak current (A) and the scan rate (V s^{-1}), A, n and ΔCo is the area of electrode (cm^2), the number of electrons for reaction and the concentration of solvated Na-ion (n=1, Co=3×10^{-3} mol cm^{-3} according to equation 1 based on $A^+(diglyme)_yC_{20}^-$ (y=2)).[S11,S12] And the values of D_{Na} for every peak could be obtained from the Figure S11 (I_p *vs* $v^{1/2}$ plots, the slope fitted from linear relation) and Table S3. As can be seen, the average D_{Na} is 2.45×10^{-10} cm^2/s.

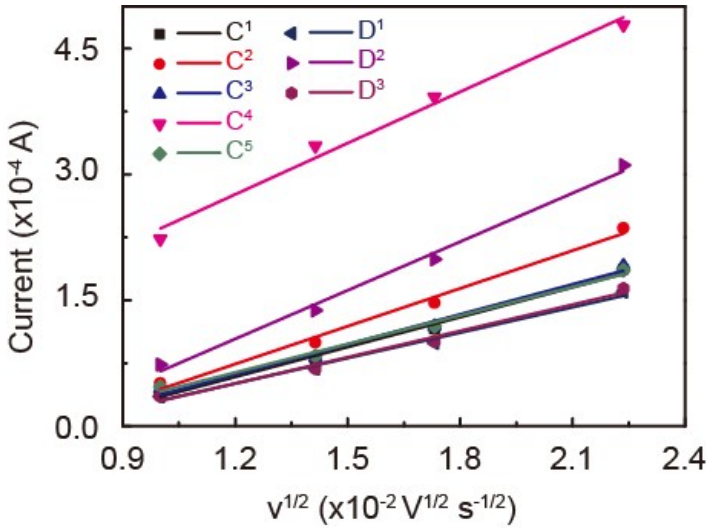

Fig. S18 Linear fittings in relation to peak value (I_p) and square root of the scan rate ($v^{1/2}$) from CV curves at 0.1, 0.2, 0.3 and 0.5 mV s^{-1}.

Table S3. The apparent diffusion coefficients of every redox peak and the average value in Na-ion half cells.

peak	slope	D ($\times 10^{-10}$ cm^2/s)
C^1	0.01184	1.69
C^2	0.01503	2.72
C^3	0.01197	1.72
C^4	0.02034	4.98
C^5	0.01128	1.53
D^1	0.01010	1.23
D^2	0.01931	4.48
D^3	0.01043	1.31
average		2.45

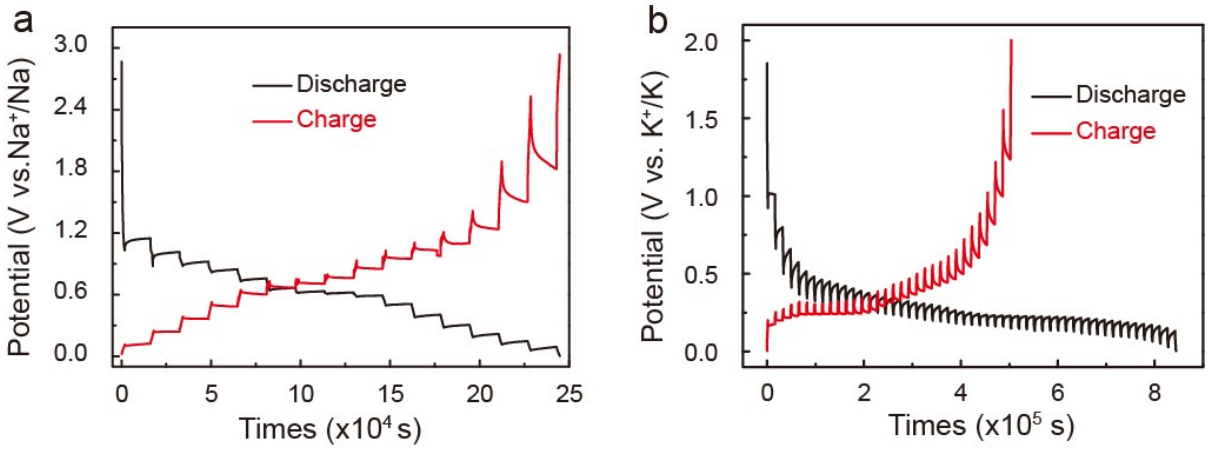

Fig. S19 GITT profiles of the second discharge/charge process for a) Na-ion half cells at 0.02 A g^{-1} between 0.01 and 2.8 V and b) K-ion half cells at 0.02 A g^{-1} between 0.01 and 2.0 V.

The apparent diffusion coefficient for solvated Na-ion and K-ion (D_{Na} and D_K) could be calculated from GITT technique based on the following equation S3, in which current density (20 mA g^{-1}) of equal duration (τ=0.5 h) were applied, followed by 4 h of relaxation period.[S11, S13]

$$D = \frac{4}{\pi\tau}\left(\frac{m_B V_M}{M_B S}\right)^2 \left(\frac{\Delta E_s}{\Delta E_\tau}\right)^2 \qquad \left(\tau \ll \frac{L^2}{D}\right) \qquad S3$$

Where m_B, V_M and M_B is the mass, molar volume and molecular weight of active material, and subsequent $V_M/M_B=\rho$ (1.44 g/cm^3 for Na-ion battery, 1.979 g/cm^3 for K-ion batteries) was figured out. The balanced voltage difference (ΔE_s) and total voltage difference ($\Delta E\tau$) during the current pulse applied in Na-ion battery were shown in Figure S20, consistent with K-ion battery.

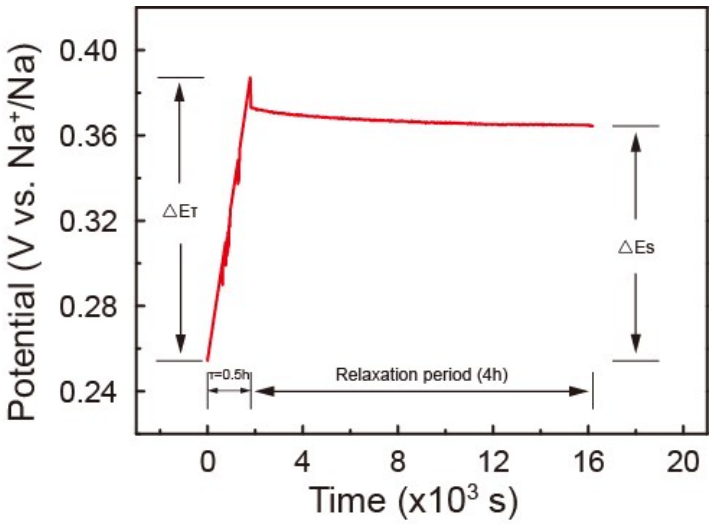

Fig. S20 The profile regarding E vs τ for a single GITT titration in Na-ion half cells.

Table S4. Electrochemical performance of RG-1300 and reported graphite anode-based NIBs.

Materials	Cyclability (mAh g^{-1})	Rate capability (mAh g^{-1})	Ref.
RG-1300	≈ 154 at 200 mA g^{-1} after 1000 cycles	≈ 162 at 200 mA g^{-1}, ≈ 135 at 5 A g^{-1}	
Graphite	≈ 96 at 37.2 mA g^{-1} after 1000 cycles	≈ 100 at 37.2 mA g^{-1}, ≈ 80 at 372 mA g^{-1}	S14
Graphite	≈ 100 at 0.5 A g^{-1} after 2500 cycles	≈150 at 100 mA g^{-1}, ≈75 at 10 A g^{-1}	S15
Graphite	≈110 at 0.2 A g^{-1} after 6000 cycles	≈110 at 0.1 A g^{-1}, ≈102 at 10 A g^{-1}	S16
Expanded graphite	115 at 0.12 A g^{-1} after 100 cycles	120 at 0.12 A g^{-1}, 78.2 at 0.24 A g^{-1}	S17
Graphene foam	≈120 at 12 A g^{-1} after 8000 cycles	≈ 150 at 1 A g^{-1}, ≈ 125 at 10 A g^{-1}	S18

Table S5. Electrochemical performance of RG-1300 and reported graphite anode-based KIBs.

Materials	Cyclability (mAh g^{-1})	Rate capability (mAh g^{-1})	Ref.
RG-1300	≈187 at 0.2 A g^{-1} after 200 cycles	320 at 50 mA g^{-1}, 252 at 200mA g^{-1}	
Graphite	≈ 250 at 28 mA g^{-1} after 50 cycles		S19
Graphite	≈140 at 20 mA g^{-1} after 100 cycles 1 M KPF6 in EC:DMC = 1:1		S20
Graphite	≈160 at 20 mA g^{-1} after 100 cycles 1 M KPF6 in EC:DEC = 1:1		S20
Graphite (solvent cointercalation)	≈95 at 2000 mA g^{-1} after 1000 cycles	80 at 10 A g^{-1}	S21
Commercial expanded graphite	228 at 50 mA g^{-1} after 200 cycles	175 at 0.2 A g^{-1}	S22

6. Supplementary references

S1. J. Shim and K. A. Striebel, *J. Power Sources*, 2007, **164**, 862-867.

S2. Y. Ein-Eli and R. Koch, *J. Electrochem. Soc.*, 1997, **144**, 2968-2973.

S3. S. Yata, H. Kinoshita, M. Komori, N. Ando, T. Kashiwarnura, T. Harada, K. Tanaka and T. Yamabe, *Synthetic Metals*, 1994, **62**, 153-158.

S4. Z. H. Zhou, M. Hibino, I. Honma, M. Ichihara, *Adv Mater.*, 2003, **15**, 2107-2111.

S5. Y. Wen, K. He, Y. Zhu, F. Han, Y. Xu, I. Matsuda, Y. Ishii, J. Cumings and C. Wang, *Nat. Commun.*, 2014, **5**, 4033.

S6. S. Hartung, N. Bucher, R. Bucher and M. Srinivasan, *Rev. Sci. Instrum.*, 2015, **86**, 086102.

S7. N. A. Cañas, P. Einsiedel, O. T. Freitag, C. Heim, M. Steinhauer, D.-W. Park and K. A. Friedrich, *Carbon*, 2017, **116**, 255-263.

S8. M.D. Levi, E.A. Levi and D. Aurbach, *J. Electroanal. Chem.*, 1997, **421**, 89-97.

S9. H. Kim, J. Hong, G. Yoon, H. Kim, K.-Y. Park, M.-S. Park, W.-S. Yoon and K. Kang, *Energy Environ. Sci.*, 2015, **8**, 2963-2969.

S10. A. Missyul, I. Bolshakov and R. Shpanchenko, *Powder Diffraction*, 2017, **32**, S56-S62.

S11. X. H. Zhang, W. L. Pang, F. Wan, J. Z. Guo, H. Y. Lu, J. Y. Li, Y. M. Xing, J. P. Zhang and X. L. Wu, *ACS Appl. Mater. Inter.*, 2016, **8**, 20650-20659.

S12. Y. H. Kwon, K. Minnici, J. J. Park, S. R. Lee, G. Zhang, E. S. Takeuchi, K. J. Takeuchi, A. C. Marschilok and E. Reichmanis, *J. Am. Chem. Soc.*, 2018, **140**, 5666-5669.

S13. Y.-Y. Wang, B.-H. Hou, J.-Z. Guo, Q.-L. Ning, W.-L. Pang, J. Wang, C.-L. Lü and X.-L. Wu, *Adv. Energy Mater.*, 2018, **8**, 1703252.

S14. B. Jache and P. Adelhelm, *Angew. Chem., Int. Ed.*, 2014, **53**, 10169-10173.

S15. H. Kim, J. Hong, Y.-U. Park, J. Kim, I. Hwang and K. Kang, *Adv. Funct. Mater.*, 2015, **25**, 534-541.

S16. Z. Zhu, F. Cheng, Z. Hu, Z. Niu and J. Chen, *J. Power Sources*, 2015, **293**, 626-634.

S17. M. Cabello, X. Bai, T. Chyrka, G. F. Ortiz, P. Lavela, R. Alcántara and J. L. Tirado, *J. Electrochem. Soc.*, 2017, **164**, A3804-A3813.

S18. A. P. Cohn, K. Share, R. Carter, L. Oakes and C. L. Pint, *Nano letters*, 2016, **16**, 543-548.

S19. S. Komaba, T. Hasegawa, M. Dahbi and K. Kubota, *Electrochem. Commun.*, 2015, **60**, 172-175.

S20. J. Zhao, X. Zou, Y. Zhu, Y. Xu and C. Wang, *Adv. Funct. Mater.*, 2016, **26**, 8103-8110.

S21. A. P. Cohn, N. Muralidharan, R. Carter, K. Share, L. Oakes and C. L. Pint, *J. Mater. Chem. A* 2016, **4**, 14954-14959.

S22. Y. An, H. Fei, G. Zeng, L. Ci, B. Xi, S. Xiong and J. Feng, *J. Power Sources*, 2018, **378**, 66-72.